Magphan® Phantoms for MR for radiation therapy and quantitative imaging applications.

Magphan® S162 & 128

Smári

Sub-voxel geometric distortion measurements and critical image quality metrics engineered for ease of use in the clinical workflow.

The Phantom Laboratory manufactures high-precision phantoms coupled with Smári image analysis service and innovative custom solutions for the medical imaging and radiation therapy fields.

Click to see our latest phantoms and schedule a demo of our Smári image analysis service.

Artificial intelligence-based framework in evaluating intrafraction motion for liver cancer robotic stereotactic body radiation therapy with fiducial tracking

Zhiwen Liang
Cancer Center, Union Hospital, Tongji Medical College, Huazhong University of Science and Technology, Wuhan 430022 Hubei, China

Qichao Zhou
Manteia Technologies Co., Ltd., Xiamen, Fujian, China

Jing Yang and Lian Zhang
Cancer Center, Union Hospital, Tongji Medical College, Huazhong University of Science and Technology, Wuhan 430022 Hubei, China

Dong Liu
Varian Medical Systems, Inc., Beijing, China

Biao Tu[a] and Sheng Zhang[a]
Cancer Center, Union Hospital, Tongji Medical College, Huazhong University of Science and Technology, Wuhan 430022 Hubei, China

Purpose: This study aimed to design a fully automated framework to evaluate intrafraction motion using orthogonal x-ray images from CyberKnife.

Methods: The proposed framework includes three modules: (a) automated fiducial marker detection, (b) three-dimensional (3D) position reconstruction, and (c) intrafraction motion evaluation. A total of 5927 images from real patients treated with CyberKnife fiducial tracking were collected. The ground truth was established by labeling coarse bounding boxes manually, and binary mask images were then obtained by applying a binary threshold and filter. These images and labels were used to train a detection model using a fully convolutional network (fCN). The output of the detection model can be used to reconstruct the 3D positions of the fiducial markers and then evaluate the intrafraction motion via a rigid transformation. For a patient test, the motion amplitudes, rotations, and fiducial cohort deformations were calculated used the developed framework for 13 patients with a total of 52 fractions.

Results: The precision and recall of the fiducial marker detection model were 98.6% and 95.6%, respectively, showing high model performance. The mean ($\pm$SD) centroid error between the predicted fiducial markers and the ground truth was 0.25 ± 0.47 pixels on the test data. For intrafraction motion evaluation, the mean ($\pm$SD) translations in the superior–posterior (SI), left–right (LR), and anterior–posterior (AP) directions were 13.1 ± 2.2 mm, 2.0 ± 0.4 mm, and 5.2 ± 1.4 mm, respectively, and the mean ($\pm$SD) rotations in the roll, pitch and yaw directions were $2.9 \pm 1.5°$, $2.5 \pm 1.5°$, and $3.1 \pm 2.2°$. Seventy-one percent of the fractions had rotations larger than the system limitations. With rotation correction during rigid registration, only 2 of the 52 fractions had residual errors larger than 2 mm in any direction, while without rotation correction, the probability of large residual errors increased to 46.2%.

Conclusion: We developed a framework with high performance and accuracy for automatic fiducial marker detection, which can be used to evaluate intrafraction motion using orthogonal x-ray images from CyberKnife. For liver patients, most fractions have fiducial cohort rotations larger than the system limitations; however, the fiducial cohort deformation is small, especially for the scenario with rotation correction. © *2020 American Association of Physicists in Medicine* [https://doi.org/10.1002/mp.14501]

1. INTRODUCTION

Stereotactic body radiation therapy (SBRT) has shown promising outcomes in the radiotherapeutic management of primary and metastatic liver cancers, such as a high local control rate.[1,2] Due to the high dose delivered per fraction, the successful administration of SBRT requires high-precision tumor localization technology, which is especially challenging considering tumor motion. To ensure tumor coverage, margins are added around the target, which are usually determined using four-dimensional (4D) computed tomography (CT) to encompass the entire movement path of the target.

However, it has been reported that 4D CT may underestimate tumor motion amplitudes[3,4] because of intrafraction motion.[5,6] Hence, intrafraction motion evaluation is essential for identifying suitable safety margins and assessing treatment delivery accuracy.

Various imaging systems have been used in the clinic for intrafraction motion evaluation, such as three-dimensional (3D)[7,8] and 4D[9,10] cone beam computed tomography (CBCT), optical systems,[11] magnetic resonance imaging (MRI),[12] ultrasound,[13] and electromagnetic transponders.[14] In terms of instantaneity, the available motion evaluation methods can be classified into two categories: offline and real-time methods. Offline methods usually rely on evaluating the differences in the intrafraction target position between post-correction and mid/post-treatment images acquired via 3D/4D CBCT or other imaging methods. Real-time methods can provide relatively accurate motion information by tracking the target position during treatments with a high temporal frequency. Real-time tracking techniques offer great potential for reducing tumor margins so as to spare surrounding normal tissues.

The CyberKnife system (Accuray, Inc., Sunnyvale, CA, USA) is one of the most commonly used devices for real-time motion tracking. Its target-locating functionality relies on a combined optical and orthogonal x-ray image system to establish a real-time correlation model during treatment. The model is then used to predict the target location and to guide the treatment. Both the model-based predicted target position and the actual target position are recorded in log files by the system. These log files can be used to evaluate the treatment accuracy[15] and intrafraction motion.[16,17] For liver patients treated with CyberKnife, fiducial markers are often implanted into patients before CT scanning, and the centroids of the fiducial markers are used for tumor tracking during treatment.[18,19] However, a limitation of this system is that some valuable data for assessing the rotation and deformation of the liver, such as the tracking results and fiducial positions, are absent in the log files.

Using x-ray images from CyberKnife seems a more direct way to reconstruct the 3D position information of the fiducial markers, which can then be used to evaluate intrafraction motion. The most challenging task is to accurately locate the positions of the fiducial markers in the x-ray images. Various methods have been proposed for automatically segmenting either cylindrical or arbitrarily shaped fiducial markers in kilovolt (kV)/megavolt (MV) fluoroscopy[20–22] or CBCT projections.[23–25] Most of these methods use the template matching approach, which requires prior information on the fiducial markers, such as their dimensions.[21] However, due to the variety of possible implantation directions, the effective dimensions can vary. In addition, the low image contrast of x-ray projections or motion of the markers may compromise the performance of fiducial marker detection.[23] Recently, Mylonas A et al.[26] adopted a convolutional neural network (CNN) model for fiducial marker detection and reported greatly improved performance compared to the traditional template matching method (sensitivity: 98.49% vs 67%, specificity:

99.96% vs 94%). The authors used a tracking window to crop an area centered on each individual marker to reduce the detection area and to reduce the difficulty of tiny object detection. This approach is effective for images collected via continuous scanning, but for the discrete x-ray images acquired by CyberKnife, the fiducial markers may easily be lost from the tracking window when handling a batch of images.

In this study, we developed a fully automated framework for analyzing intrafraction motion using orthogonal kV x-ray images acquired with CyberKnife. The framework includes a fully convolutional network (fCN)-based fiducial marker detection module, a 3D position reconstruction module and a quantitative intrafraction motion evaluation module. The proposed framework was tested on 13 patients to demonstrate its effectiveness in assessing intrafraction tumor motion.

2. MATERIALS AND METHODS

The overall framework for intrafraction motion analysis is presented in Fig. 1. All image pairs from a fraction acquired using the orthogonal x-ray imaging system of CyberKnife are input into the fiducial detection model. For each image pair, the output coordinates of the fiducial cohort in the two-dimensional (2D) images are used to reconstruct the 3D positions via a transformation matrix. Then, the resulting lists of 3D positions ($M_{i,k}(x,y,z)$) are input into the intrafraction motion evaluation module for calculating translations, rotations, and residual errors.

The key component of the framework is the fiducial detection model, which is an fCN-based deep learning model and needs prior training (Section 2.A). The other components, namely, the 3D position reconstruction and intrafraction motion estimation modules, are an extension of our previous work[27] and will be summarized in Sections 2.B and 2.C, respectively.

2.A. Deep learning network for fiducial marker detection

2.A.1. Training data preprocessing

The data used to train the deep learning network were acquired from real liver patients using the x-ray imaging system of CyberKnife. They are 16-bit grayscale images with a 512×512 pixel resolution. The fiducial markers used at our center are cylindrical, with a length of 3 mm and a diameter of 0.5 mm, and each marker occupies only approximately 10 pixels in an image. All fiducial markers were first annotated manually with coarse bounding boxes. Then, two procedures were performed to obtain the ground-truth binary mask images, as follows.

1. Binary threshold segmentation.

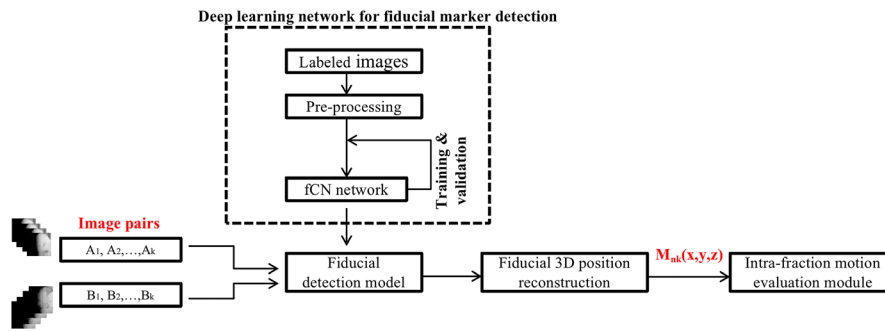For each bounding box, a threshold was defined for segmenting the fiducial marker:

FIG. 1. The workflow of the framework. The image pairs (A_i, B_i) are the images acquired by the CyberKnife imaging system (detector A and detector B). The lowercase i denotes the ith image pair. $M_{i,k}(x, y, z)$ denotes the coordinates of the kth fiducial marker in the ith image pair. [Color figure can be viewed at wileyon linelibrary.com]

$$\text{Threshold} = I_{max} - 1.8 \times I_{std} \tag{1}$$

where I_{max} and I_{std} are the maximum intensity and the standard deviation of the intensity, respectively, within the bounding box.

Inside the bounding box, if the intensity of a pixel is higher than the threshold, it was set to 1; otherwise, it was set to 0. The pixels outside the bounding boxes were all set to 0.

2. Small cluster removal. Any clusters containing fewer than 8 pixels were removed by a filter.

2.A.2. Network architecture

In this study, we trained a U-Net, which is a variant of an fCN, to segment the fiducial markers. The fCN architecture was the first network architecture developed for semantic pixelwise segmentation, with three main characteristics: (a) fully connected layers are replaced with convolutional layers to adapt the model for inputs of arbitrary size; (b) in-network upsampling is adopted to produce correspondingly sized output; and (c) skip connections are used to maintain accuracy and robustness. The U-Net architecture (Fig. 2) has a symmetrical encoder–decoder structure and is commonly used for medical images.[28] It consists of a contracting path to capture context, a symmetrical expanding path to map the low-resolution encoder feature maps to full-input-resolution feature maps, and skip connections to improve the model's accuracy and address the vanishing gradient problem. On each step of the contracting path, double 3×3 convolutions with [1, 1] padding are used to maintain the spatial resolution. Each convolution is followed by batch normalization and rectified linear unit (ReLU) activation to reduce the variance and increase the stability of the network. Then, 2×2 max pooling with stride 2 is used for downsampling. On every step of the expanding path, we use a 2×2 upconvolution for upsampling and halve the number of channels. The skip connections take the cropped feature maps from the contracting path and concatenate them with the corresponding upsampled feature maps. After two 3×3 convolution blocks, upsampling is performed again. In the output layer, a 1×1 convolution is used to reduce the number of feature map channels to 1, and the sigmoid function is used to calculate the membership probability of each pixel. Thus, the output of the network is a binary mask of the same size as the input image.

2.A.3. Model training and evaluation

A model with the architecture introduced above was trained on a personal computer (PC) with an Intel Core i7-7700K CPU (4.2 GHz), 32 GB of memory and an NVIDIA GTX 1080 Ti graphics card. A total of 5927 images from real patients were used to build the model, with 2943 images used as the training set, 1542 images used as the validation set and 1442 images used as the test set. The adaptive moment estimation (Adam) optimizer was used to minimize the loss function, which is shown in Eqs. (2) and (3). The learning rate and the batch size were set to 0.0001 and 6, respectively.

$$\text{loss} = -\ln(\text{Dice}) \tag{2}$$

$$Dice = \frac{2(A \cap B)}{A + B} \tag{3}$$

where A is the ground truth and B is the predicted binary mask.

The precision and recall values were used to quantify the performance of the model. The precision is the percentage of true positives among the model-detected fiducial markers. The recall is the percentage of true positives among the total number of fiducial markers. These two indexes are defined as shown in Eqs. (4) and (5), respectively.

$$Precision = \frac{TP}{TP + FP} \tag{4}$$

$$Recall = \frac{TP}{TP + FN} \tag{5}$$

where TP is the number of true positives, FP is the number of false positives, and FN is the number of false negatives.

The true positives are the fiducial markers that are correctly detected. To recognize the true positives, the small clusters in the predicted binary mask were first removed, and this binary mask was then cropped into separate areas, each containing one predicted fiducial marker. The Dice coefficients were calculated for each individual fiducial marker.
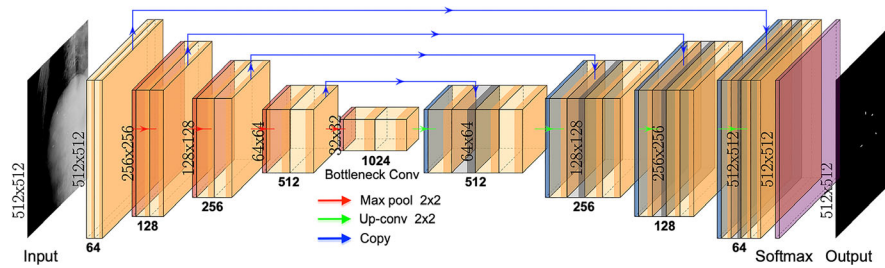
FIG. 2. Architecture of the network for fiducial marker segmentation. It consists of a contracting path and an expanding path. Each box corresponds to a multi-channel feature map. For each feature map, the numbers on the left side of the box represent the size, and that on the bottom of the box denotes the number of channels. The arrows denote different operations. The blue arrows represent skip connections with a copy operation. The red and green arrows denote downsampling and upsampling, respectively. [Color figure can be viewed at wileyonlinelibrary.com]

Markers with Dice coefficients higher than a given Dice threshold were considered true positives. Accordingly, it was necessary to choose a proper Dice threshold to balance the trade-off between detection ability and position accuracy.

Considering that the 3D position reconstruction module requires the fiducial coordinates as input, all detected fiducial markers were represented by bounding boxes. The centroids of the bounding boxes were used to define the coordinates of the fiducial markers.

2.B. 3D position reconstruction

The 3D coordinates of a point can be reconstructed from the coordinates of the corresponding points in two projections. Suppose that a fiducial marker is positioned at the point M in the patient coordinates (x, y, z) and that the projections of M in the two detectors are P_A, at (u_a, v_a), and P_B, at (u_b, v_b). Then, the 3D coordinates of point M can be derived from the coordinates of points P_A and P_B using Eq. (6). In this study, P_A and P_B are the outputs of the detection model. In accordance with the geometric configuration of the Cyber-Knife imaging system (Fig. S1), θ is π/4.

$$\begin{pmatrix} x \\ y \\ z \end{pmatrix} = \begin{pmatrix} \cos\theta & -\sin\theta & 0 \\ \sin\theta & \cos\theta & 0 \\ 0 & 0 & 1 \end{pmatrix} \begin{pmatrix} u_a \\ u_b \\ (v_a + v_b)/2 \end{pmatrix} \quad (6)$$

2.C. Intrafraction motion evaluation

The input data to the intrafraction motion evaluation module consist of a list of the 3D positions of each fiducial marker in each image pair. Four steps are applied in this module for calculation.

1. Outlier detection. Tukey's box-plot method[29] is used to remove outliers.
2. Fiducial cohort registration. The aim of the registration process is to find an optimal rigid transformation between the floating fiducial cohort and the reference fiducial cohort. For a fiducial cohort that contains K fiducial markers, the floating and reference fiducial cohorts are denoted by P = {p_1, p_2,..., p_k} and

Q = {q_1, q_2,..., q_k}, respectively. The rigid transformation has six degrees of freedom (three rotations and three translations), which are expressed by a rotation matrix (R) and a translation vector (T). If only translations are needed, R will be the identity matrix. The iterative closest point (ICP) algorithm[30] is used to minimize the cost function [Eq. (7)] of the six-dimensional (6D) rigid registration problem.

$$\arg\min \sum_{i=1}^{K} ||Rp_i + T - q_i||^2 \quad (7)$$

3. Residual error calculation. The residual error is the Euclidean distance between corresponding fiducial markers in the floating and reference fiducial cohorts after the 6D rigid registration. Defining the residual error in this way will be beneficial for calculating the expansion of the isotropic planning target volume in the future. The residual errors with and without rotation correction can be calculated by changing the form of R.
4. Intrafraction motion estimation. The motion amplitudes, rotations, and deformation of the fiducial cohort are used to represent the overall intrafraction motion. The amplitudes and rotations are defined as the 5% to 95% percentiles of the ranges of translations and rotations in the fraction. The fiducial cohort deformation is defined as the maximum residual error in the fraction.

2.D. Patient study

Before testing with clinical data, the scaling factor (= 0.32 mm/pixel) for converting the distance on the images to physical dimensions in the real world was determined with an automated quality assurance (AQA) phantom. The geometric accuracy of the first two modules of proposed framework was verified with a Baby Blue phantom (Standard Imaging, WI, USA). More detailed information can be found in Figs. S2 and S3.

Data from 13 liver patients with a total of 52 fractions were used to test the framework and evaluate the intrafraction target motion. For each patient, at least three fiducial markers

were implanted near the tumor. Based on Couinaud's segmentation of the CT images, the liver was divided into eight sections, and the tumors considered in this study were located in sections IV–VIII (Fig, S4). The median volume of these tumors was 19 cc (range: 4–189 cc).

The motion amplitudes, rotations, and deformations of the fiducial cohort were calculated using the developed framework for these liver cases. For comparison, the motion amplitudes were also calculated from the position information stored in the system log files. The Wilcoxon signed-rank test was applied to compare these two sets of amplitudes to assess the feasibility of using x-ray images for intrafraction motion evaluation. The same test was also performed to compare the fiducial cohort deformations calculated with and without rotation correction, respectively.

3. RESULTS

3.A. Performance of the detection model

Figure 3 shows the evolution of the loss and the Dice coefficient over consecutive epochs of the training and validation processes. The training process clearly converged smoothly. At the end of the curves, the training loss and Dice coefficient are still decreasing/increasing, respectively, while no significant change in the validation loss and Dice coefficient can be observed. Therefore, an early stopping strategy was adopted to avoid overfitting and stop the training process. In the inference stage, 57 ms were required to apply the detection model to each image.

Because the Dice threshold can affect the performance and accuracy of the detection model, the precision, recall and centroid differences between the predictions and ground truth were calculated with full range of Dice threshold values (Fig. 4). Unexpectedly, the centroid differences remained at the subpixel level as the Dice threshold was varied from 0.9 to 0.1, while the model performance in terms of precision and recall increased from 87.2% to 99.6% and from 84.5% to 97.4%, respectively. This is because most of the fiducial markers had high Dice coefficients. For example, for a Dice threshold of 0.7, the 95.6% recall means that 95.6% of the fiducial markers have Dice coefficients larger than 0.7.

Consequently, when we decrease the Dice threshold from 0.7 to 0.1, improvements of only 1% and 1.8% can be achieved in terms of precision and recall, respectively. Hence, a Dice coefficient of 0.7, which is clinically acceptable for tiny objects such as fiducial markers, was chosen. The corresponding precision and recall were 98.6% and 95.6%, respectively, and the mean ($\pm$SD) centroid error between the predicted and ground-truth fiducial markers was 0.25 ± 0.47 pixels. Examples of corresponding results derived from the detection model are shown in Fig. 5. The predicted bounding boxes match the fiducial markers perfectly.

3.B. Intrafraction motion evaluation for liver cases

Table I shows the mean ($\pm$SD) motion amplitudes and rotations across all fractions and all patients. No significant differences between the x-ray image-based amplitudes and the log file-based amplitudes were found by the Wilcoxon signed-rank test (all $P > 0.05$), indicating that the results calculated using the developed framework are reliable and can be used for intrafraction motion evaluation. For the Cyber-Knife system, the magnitudes of the maximum rotational corrections that it can apply during treatment with Synchrony fiducial tracking are $\pm 1.5°$ for the roll and pitch directions and $\pm 3.0°$ for the yaw direction.[18] From Table I, we can also observe that the largest rotation was in the yaw direction, although this is not always the case for individual patients. Our results show that among all 52 fractions, 40%, 54%, and 6% exhibited rotations that exceeded the system's limitations in the roll, pitch and yaw directions, respectively, thus requiring tracking to be performed without rotation correction. The overall percentage of fractions with rotations exceeding the limitations in at least one direction was 71%.

Table II lists the mean ($\pm$SD) fiducial cohort deformations with and without rotation correction. The results of the Wilcoxon signed-rank test (all $P < 0.001$) indicated that the residual errors with rotation correction were significantly lower than those without rotation correction. Only two fractions showed residual errors larger than 2 mm in any direction for the scenario with rotation correction, while without rotation correction, the probability of large residual errors increased to 46.2%.
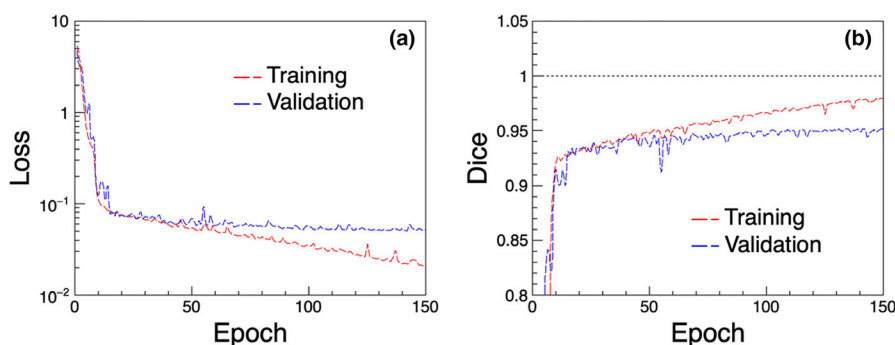

FIG. 3. Training and validation loss (a) and Dice coefficient (b) as functions of the epoch for the fiducial detection model. After 100 epochs, the validation loss and Dice coefficient begin to level off. [Color figure can be viewed at wileyonlinelibrary.com]
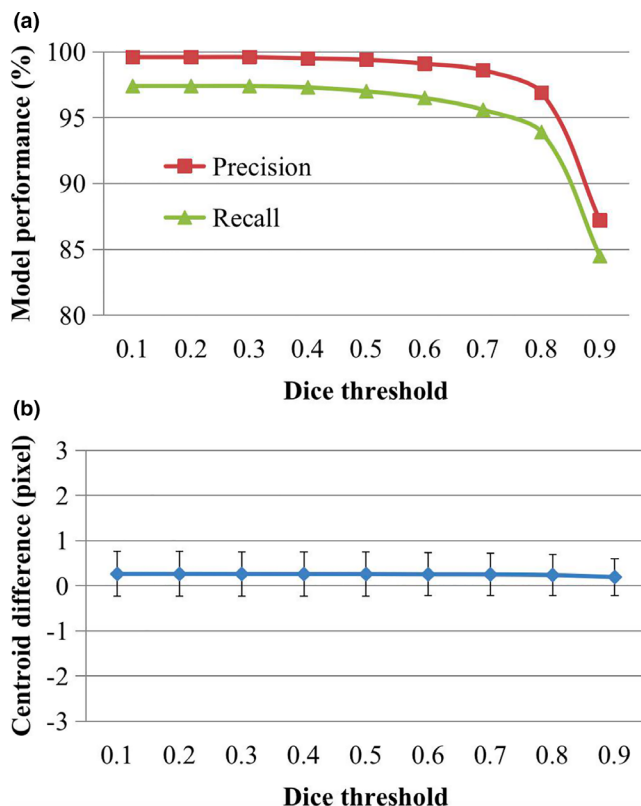
FIG. 4. Model performance (a) and centroid differences (b) at different Dice thresholds. Each point in (b) is the mean centroid difference between the predicted and ground-truth fiducial markers at the corresponding Dice threshold for the test data, and the error bars represent the standard deviations of the centroid differences. [Color figure can be viewed at wileyonlinelibrary.com]

4. DISCUSSION

In this work, we developed an artificial intelligence-based fully automated framework for evaluating intrafraction motion using discrete x-ray images from CyberKnife. Although functionalities for finding and tracking fiducial markers are provided by the vendors of CyberKnife, they do not provide a convenient tool for analyzing the intrafraction motion of the fiducial markers, which is very important for evaluating uncertainties and quantifying the safety margin. Moreover, the proposed artificial intelligence-based method has the potential to be extended to more complicated tasks, such as real-time tumor tracking or spine tracking, and applications, such as automatic patient setup, with further advancements in the capabilities of graphics processing units (GPUs).

Distinct from other existing techniques, our method utilizes the U-Net architecture and full-size images for pixelwise fiducial marker detection. The method is inspired by the work of Cheng et al.,[31] who introduced segmentation directly into detection to avoid the defects introduced by the well-known approaches of region proposal networks (RPNs) and nonmaximum suppression (NMS), in which it is not possible to obtain a threshold that is appropriate for all images. By comparison with other methods (Appendix A), the benefits of our method are threefold. First, no postprocessing, such as NMS,

is required to obtain acceptable results. Second, unlike the template matching approach, our method does not require prior information on the fiducial markers. Third, pixelwise detection is particularly suitable for detecting small objects in large-scale scenes. It is worth noting that although our fiducial marker detection model achieved a high precision of 98.6% and a recall of 95.6% in this study, a small probability of false detection or missed detection was observed during testing. Therefore, when evaluating intrafraction motion, all of the detected fiducial markers were carefully checked and corrected to ensure the accuracy of intrafraction motion evaluation.

Until recently, few publications have reported fiducial cohort rotations and residual tracking errors.[32] In addition to the difficulty of obtaining rotation and residual error information, the rotation limitations of the CyberKnife system result in a large number of patients being treated based on fewer than three fiducial markers in general. Using the proposed framework, we found that the roll and pitch limitations in particular are too strict (only $\pm 1.5°$), resulting in 40% and 54% of fractions, respectively, having rotations larger than the system limitations. Overall, the probability of exceeding the system's rotation limitations in at least one direction increases to 71%. These results are very close to those of Ming Liu et al., who reported that rotation correction was impossible for 92% of patients due to imperfect fiducial implantation and system limitations.[18] It seems that it may not be possible to perform rotation correction for the majority of fractions in liver cases. Unfortunately, without a rotation correction strategy during treatment, a larger planning target volume (PTV) margin is needed because the fiducial cohort deformation has a 46.2% probability of being larger than 2 mm.

CyberKnife is able to track a moving target under the assumption that the fiducial cohort should have rigid-body motion only, which means that the target and surrounding tissue should not have significant deformation. However, liver itself is a deformable organ, and the physiological/mechanical pressure, respiratory-induced motion, digestion, and filling of the bladder and rectum may all cause this assumption to be broken. Our results (Table II) prove that the fiducial cohort indeed exhibits limited deformation for liver cases in most fractions, especially for treatment with rotation correction. However, it should be noted that these results may be biased because patients with tumors located in Sections 1–3 of the liver were not included in this study.

Another interesting observation is that the results seem to be correlated with the imaging modality used for analysis. Similar results were demonstrated by Xu et al.[33] using the same imaging modality as we used and by Bertholet et al.[32] using 2D CBCT projections, while larger intermarker deformations have been observed in 4D CT.[34] In our opinion, in 4D CT, the positions of fiducial markers can be affected by various factors, such as artifacts, irregular patient breathing, and the reconstruction algorithm and sorting method used. In contrast, CyberKnife x-ray images and 2D CBCT projections are arguably more reliable in terms of representing the instantaneous positions of fiducial markers.
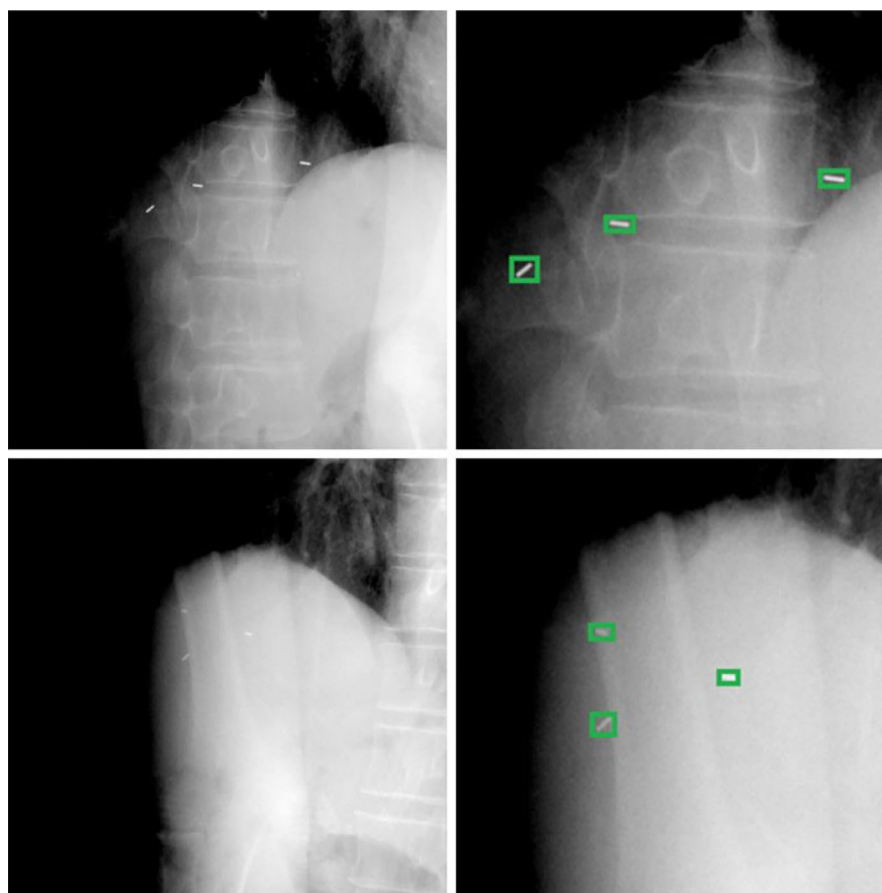
FIG. 5. Sample images with detected fiducial markers. The images in the upper and lower left are pair of images from the same patient. The images in the upper and lower right are corresponding enlarged views taken from these images, and the green boxes are the predicted bounding boxes. The centroid of each bounding box corresponds to the fiducial coordinates. [Color figure can be viewed at wileyonlinelibrary.com]

TABLE I. Mean (±SD) motion amplitudes and rotations for all fractions. (a) and (b) are the amplitudes derived from the orthogonal x-ray images and the log files, respectively. Difference = (a)–(b). CyberKnife log files do not provide rotational corrections.

	Imaging-based[a]	Log file-based[b]	Difference	*P* value
Amplitudes (mm)				
SI	13.1 ± 2.2	13.6 ± 4.8	−0.5 ± 1.8	0.088
LR	2.0 ± 0.4	2.3 ± 1.6	−0.4 ± 0.8	0.241
AP	5.1 ± 0.8	4.8 ± 2.3	0.1 ± 1.2	0.067
Rotations (°)				
Roll	2.9 ± 1.5			
Pitch	2.5 ± 1.5			
Yaw	3.1 ± 2.2			

TABLE II. Mean (±SD) fiducial cohort deformations with and without rotation correction for all fractions (mm). (a) and (b) are the residual errors with and without rotation correction, respectively. Difference = (a)–(b).

	With rotation correction (a)	Without rotation correction (b)	Difference	*P* value
SI	0.6 ± 0.5	1.6 ± 0.6	−0.9 ± 0.7	0
LR	0.4 ± 0.2	1.7 ± 1.0	−1.2 ± 1.0	0
AP	0.5 ± 0.2	1.0 ± 0.5	−0.5 ± 0.5	0

for intrafraction motion evaluation. Based on our research results, the intrafraction motion of fiducial cohorts often exhibits rotations larger than the system limitations of CyberKnife. However, our observations show that the deformations of fiducial cohorts are insignificant when compared with rotation correction data.

5. CONCLUSION

In this paper, we developed a framework for automated fiducial marker detection and intrafraction motion evaluation using orthogonal x-ray images from CyberKnife. The proposed fiducial marker detection method based on an fCN (U-Net) model was tested and demonstrated improved efficiency

CONFLICT OF INTEREST

The authors have no relevant conflict of interest to disclose.

Zhiwen Liang and Qichao Zhou contributed equally to this paper.

a)Authors to whom correspondence should be addressed. Electronic mails: tubiao@hust.edu.cn, tonydppx@hotmail.com; Telephones: 86-13971442699, 86-13971442699; Fax: 86-27-6565 0733.

REFERENCES

1. Scorsetti M, Arcangeli S, Tozzi A, et al. Is stereotactic body radiation therapy an attractive option for unresectable liver metastases? A preliminary report from a phase 2 trial. *Int J Radiat Oncol Biol Phys*. 2013;86:336–342.

2. Yamashita H, Onishi H, Matsumoto Y, et al. Local effect of stereotactic body radiotherapy for primary and metastatic liver tumors in 130 Japanese patients. *Radiat Oncol*. 2014;9:112.

3. Harada K, Katoh N, Suzuki R, et al. Evaluation of the motion of lung tumors during stereotactic body radiation therapy (SBRT) with four-dimensional computed tomography (4DCT) using real-time tumor-tracking radiotherapy system (RTRT). *Phys Med*. 2016;32:305–311.

4. Steiner E, Shieh C-C, Caillet V, et al. Both four-dimensional computed tomography and four-dimensional cone beam computed tomography under-predict lung target motion during radiotherapy. *Radiother Oncol*. 2019;135:65–73.

5. Takao S, Miyamoto N, Matsuura T, et al. Intrafractional baseline shift or drift of lung tumor motion during gated radiation therapy with a real-time tumor-tracking system. *Int J Radiat Oncol Biol Phys*. 2016;94: 172–180.

6. Liang Z, Yang J, Liu H, et al. Real-time tumor motion monitoring and PTV margin determination in lung SBRT treatment. *Acta Oncol*. 2019;58:1786–1789.

7. Case RB, Sonke JJ, Moseley DJ, Kim J, Brock KK, Dawson LA. Inter- and intrafraction variability in liver position in non-breath-hold stereotactic body radiotherapy. *Int J Radiat Oncol Biol Phys*. 2009;75:302–308.

8. Purdie TG, Bissonnette JP, Franks K, et al. Cone-beam computed tomography for on-line image guidance of lung stereotactic radiotherapy: localization, verification, and intrafraction tumor position. *Int J Radiat Oncol Biol Phys*. 2007;68:243–252.

9. Purdie TG, Moseley DJ, Bissonnette JP, et al. Respiration correlated cone-beam computed tomography and 4DCT for evaluating target motion in stereotactic lung radiation therapy. *Acta Oncol*. 2006;45: 915–922.

10. Michalski D, Sontag M, Li F, et al. Four-dimensional computed tomography-based interfractional reproducibility study of lung tumor intrafractional motion. *Int J Radiat Oncol Biol Phys*. 2008;71:714–724.

11. Zagar TM, Kaidar-Person O, Tang X, et al. Utility of deep inspiration breath hold for left-sided breast radiation therapy in preventing early cardiac perfusion defects: a prospective study. *Int J Radiat Oncol Biol Phys*. 2017;97, 903–909.

12. Eccles CL, Patel R, Simeonov AK, Lockwood G, Haider M, Dawson LA. Comparison of liver tumor motion with and without abdominal compression using cine-magnetic resonance imaging. *Int J Radiat Oncol Biol Phys*. 2011;79:602–608.

13. Grimwood A, McNair HA, O'Shea TP, et al. In vivo validation of elekta's clarity autoscan for ultrasound-based intrafraction motion estimation of the prostate during radiation therapy. *Int J Radiat Oncol Biol Phys*. 2018;102:912–921.

14. Schmitt D, Nill S, Roeder F, Gompelmann D, Herth F, Oelfke U. Motion monitoring during a course of lung radiotherapy with anchored electromagnetic transponders : quantification of inter- and intrafraction motion and variability of relative transponder positions. *Strahlenther Onkol*. 2017;193:840–847.

15. Hoogeman M, Prevost JB, Nuyttens J, Poll J, Levendag P, Heijmen B. Clinical accuracy of the respiratory tumor tracking system of the cyberknife: assessment by analysis of log files. *Int J Radiat Oncol Biol Phys*. 2009;74:297–303.

16. Knybel L, Cvek J, Molenda L, Stieberova N, Feltl D. Analysis of lung tumor motion in a large sample: patterns and factors influencing precise delineation of internal target volume. *Int J Radiat Oncol Biol Phys*. 2016;96:751–758.

17. Liang Z, Liu H, Xue J, et al. Evaluation of the intra- and interfractional tumor motion and variability by fiducial-based real-time tracking in liver stereotactic body radiation therapy. *J Appl Clin Med Phys*. 2018;19:94–100.

18. Liu M, Cygler JE, Vandervoort E. Geometrical tracking accuracy and appropriate PTV margins for robotic radiosurgery of liver lesions by SBRT. *Acta Oncol*. 2019;58:906–915.

19. Chan M, Grehn M, Cremers F, et al. Dosimetric implications of residual tracking errors during robotic SBRT of liver metastases. *Int J Radiat Oncol Biol Phys*. 2017;97:839–848.

20. Chi Y, Shen C, Li B, et al. A method to reconstruct intra-fractional liver motion in rotational radiotherapy using linear fiducial markers. *Phys Med Biol*. 2019;64:225013.

21. Fledelius W, Worm E, Hoyer M, Grau C, Poulsen PR. Real-time segmentation of multiple implanted cylindrical liver markers in kilovoltage and megavoltage x-ray images. *Phys Med Biol*. 2014;59:2787–2800.

22. Wan H, Ge J, Parikh P. Using dynamic programming to improve fiducial marker localization. *Phys Med Biol*. 2014;59:1935–1946.

23. Fledelius W, Worm E, Elstrom UV, et al. Robust automatic segmentation of multiple implanted cylindrical gold fiducial markers in cone-beam CT projections. *Med Phys*. 2011;38:6351–6361.

24. Poulsen PR, Fledelius W, Keall PJ, et al. A method for robust segmentation of arbitrarily shaped radiopaque structures in cone-beam CT projections. *Med Phys*. 2011;38:2151–2156.

25. Bertholet J, Wan H, Toftegaard J, et al. Fully automatic segmentation of arbitrarily shaped fiducial markers in cone-beam CT projections. *Phys Med Biol*. 2017;62:1327–1341.

26. Mylonas A, Keall PJ, Booth JT, et al. A deep learning framework for automatic detection of arbitrarily shaped fiducial markers in intrafraction fluoroscopic images. *Med Phys*. 2019;46:2286–2297.

27. Li WZ, Liang ZW, Cao Y, et al. Estimating intrafraction tumor motion during fiducial-based liver stereotactic radiotherapy via an iterative closest point (ICP) algorithm. *Radiat Oncol*. 2019;14:185.

28. Ronneberger O, Fischer P, Brox T. U-Net: Convolutional Networks for Biomedical Image Segmentation. arXiv e-prints. 2015.arXiv:1505.04597. https://ui.adsabs.harvard.edu/abs/2015arXiv150504597R Accessed May 01, 2015.

29. Potter K. Methods for presenting statistical information: The box plot. In Hans Hagen, Adnreas Kerren, and Peter Dannenmann (Eds.), Visualization of Large and Unstructured Data Sets, 2008; GI-Edition Lecture Notes in Informatics (LNI) S-4:97–106.

30. Tehrani JN, O'Brien RT, Poulsen PR, Keall P. Real-time estimation of prostate tumor rotation and translation with a kV imaging system based on an iterative closest point algorithm. *Phys Med Biol*. 2013;58: 8517–8533.

31. Cheng Z, Wu Y, Xu Z, Lukasiewicz T, Wang W. Segmentation is All You Need. arXiv e-prints; 2019. https://ui.adsabs.harvard.edu/abs/2019arXiv190413300C Accessed April 01, 2019.

32. Bertholet J, Worm ES, Fledelius W, Hoyer M, Poulsen PR. Time-resolved intrafraction target translations and rotations during stereotactic liver radiation therapy: implications for marker-based localization accuracy. *Int J Radiat Oncol Biol Phys*. 2016;95:802–809.

33. Xu Q, Hanna G, Grimm J, et al. Quantifying rigid and nonrigid motion of liver tumors during stereotactic body radiation therapy. *Int J Radiat Oncol Biol Phys*. 2014;90:94–101.

34. Paulsson AK, Yom SS, Anwar M, et al. Is the liver a static organ: intraorgan deformation quantified through fiducial displacement on 4DCT. *Intl J Radiat Oncol Biol Phys*. 2015;93:E616.

SUPPORTING INFORMATION

Additional supporting information may be found online in the Supporting Information section at the end of the article.

Data S1. Supplementary Figures (S1–S4).
Appendix A. Performance comparison.